Operation of a Bidirectional Series-Resonant Converter With Minimized Tank Current and Wide ZVS Range

Song Hu, *Student Member, IEEE*, Xiaodong Li, *Senior Member, IEEE*, and Ashoka K. S. Bhat, *Fellow, IEEE*

***Abstract*—Due to wide soft-switching operation range, high-frequency isolated resonant converters are featured with low switching losses. Therefore, it is meaningful to minimize the resonant tank current in an isolated resonant converter in order to enhance the overall system efficiency. In this work, a bidirectional series-resonant converter under phase-shifted modulation combined with a modified pulsewidth modulation gating scheme is addressed. The modified pulsewidth modulation gating scheme is helpful to keep more switches operating in zero-voltage switching (ZVS) at light load. According to the steady-state analysis with the fundamental harmonic approximation approach, a specified control strategy with minimum rms tank current based on three control dimensions is proposed in closed form. The validity of the proposed control strategy is verified through experimental tests. The pulsewidth of modulated voltage using the modified gating scheme is larger than that of the conventional pulsewidth modulation voltage, which compensates for the effects of more high-order harmonics on rms current. Therefore, compared with existing control strategies for minimum current operation, the proposed control strategy demonstrates comparable performance in depressing conduction loss and wider soft-switching range in high load range. And it is able to achieve higher efficiency at light load, thanks to more switches working in ZVS.**

***Index Terms*—DC–DC converter, pulsewidth modulation (PWM), resonant converter.**

NOMENCLATURE

δ_x	On-time duration of S_2 and S_4 in one HF period.
δ_y	On-time duration of Q_2 and Q_4 in one HF period.
ϕ	Phase shift between S_2 and Q_2.
G	Load percentage or load level.
i_t	Resonant tank current.
L_s, C_s	Resonant inductance and capacitance.
M	Voltage gain.

Manuscript received November 5, 2017; revised February 12, 2018; accepted March 15, 2018. Date of publication March 21, 2018; date of current version November 19, 2018. This work was supported by the Science and Technology Development Fund of Macau under Grant 004/2015/A1. Recommended for publication by Associate Editor L. Corradini. *(Corresponding author: Xiaodong Li.)*

S. Hu and X. Li are with the Faculty of Information Technology, Macau University of Science and Technology, Macau, China (e-mail:

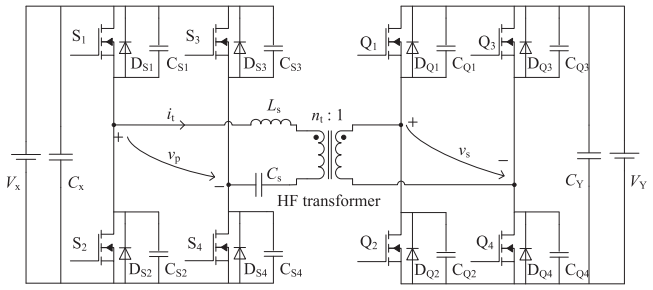

Fig. 1. Circuit diagram of a DBSRC.

may maintain ZVS operation increases to six at the variation of converter gain and load level. In [22], a new pulsewidth control scheme was proposed, in which the resulted HF ac voltage has two consecutive pulses with opposite polarity and only one null time duration in each HF period. Since the pulsewidth is adjusted from one side of the ac voltage, in this paper, the scheme is named as asymmetric-adjusted PWM (AAPWM). It enables the full bridge to keep up to three switches in ZVS operation when the pulsewidth is narrow [22]–[27]. It is reported that the AAPWM is utilized in one bridge and combined with PSM for the control in a DBSRC [28], and seven out of the total eight switches may keep ZVS operation in a wide operation range. However, no specified control strategy for the two-dimensional control scheme is given for the variation of load and converter gain. Besides, comparisons with other optimized control strategies reported for a DBSRC are not available in the literature. In this paper, AAPWM will be applied to both bridges in a DBSRC and combined with PSM to form a three-dimensional control scheme. A steady-state analysis using fundamental harmonic approximation (FHA) approach will be performed in Section II. By minimizing the obtained resonant tank current, a control strategy based on the three control variables will be developed, and a series of closed-form solutions are given. Experimental validation of the proposed control strategy is reported in Section III, and comparisons with PSM and MCT strategies are also carried out.

II. Operation Principle and Steady-State Analysis With PSM Plus AAPWM Control

The circuit schematic of an HF-isolated DBSRC is shown in Fig. 1. It employs a nearly symmetric structure with two H-bridge circuits isolated by an *LC*-type resonant tank and an HF transformer. Each bridge is implemented by four power switches with their antiparallel body diodes. The capacitors across the switches are snubber capacitors or switch parasitic capacitors. The symmetric structure enables two voltage sources $V_{\rm X}$ and $V_{\rm Y}$ to exchange energy bidirectionally. $C_{\rm X}$ and $C_{\rm Y}$ are filter capacitors on two sides, respectively. The gating scheme of AAPWM used in this work can be understood by referring to the steady-state waveforms shown in Fig. 2. Two switches in each bridge arm should be operated complementarily with necessary deadband to prevent any risk of short circuit. The cross-opposite switches S_2 and S_3 on the primary side are always turned ON at same time, so are switches Q_2 and Q_3 on the secondary side. On

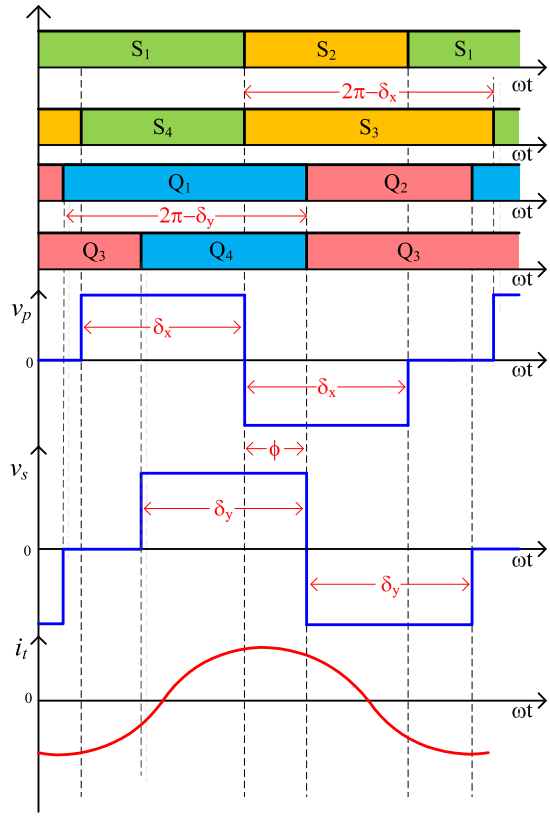

Fig. 2. Steady-state waveforms with PSM and AAPWM control for positive power transfer.

the primary side, the ON-time duration of two low-side switches S_2 and S_4 in one HF period is defined as δ_x and the ON-time duration of two high-side switches S_1 and S_3 in one HF period is $2\pi - \delta_x$, On the secondary side, the ON-time duration of two low-side switches Q_2 and Q_4 in one HF period is defined as δ_y and the ON-time duration of two high-side switches Q_1 and Q_3 in one HF period is $2\pi - \delta_y$. Both δ_x and δ_y are assumed to be less than or equal to π. Besides, there is a phase angle ϕ by which the turn-ON moment of S_2 and S_3 leads the turn-ON moment of Q_2 and Q_3. As a result, the obtained two HF ac voltages v_p and v_s have quasi-square-wave form with modified adjustable pulsewidth δ_x and δ_y, respectively, and there is only one zero-voltage portion in each HF period.

Due to the near resonance operation, the FHA approach can be used for the steady-state analysis of this resonant converter with an acceptable accuracy. The assumptions used in FHA analysis are as follows. All switches and diodes are assumed to be ideal. The magnetizing inductance of the HF transformer is assumed to be infinite. The leakage inductance of the HF transformer can be regarded as part of the resonant inductance. The effects of snubber capacitors and the deadband in gating signals are neglected. For the purpose of convenience, all quantities will be normalized with the following base values and the superscript "N" is used to represent a normalized value:

$$V_B = V_X \quad Z_B = \frac{n_t^2 V_Y^2}{P_{\rm rate}} \quad \omega_B = \sqrt{(L_s C_s)^{-1}} \qquad (1)$$

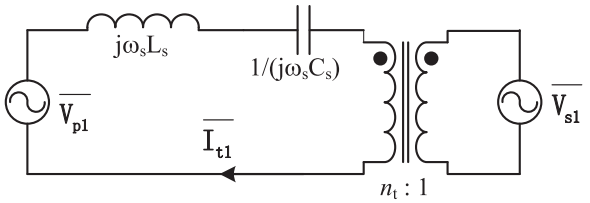

Fig. 3. Equivalent circuits for fundamental components in the phasor domain.

where P_{rate} is the rated power and n_t:1 is the turn ratio of the HF transformer. The normalized switching frequency is defined as $F = \omega_s/\omega_B$. The normalized impedance of the resonant tank is $X_{sN} = (\omega_s L_s - \frac{1}{\omega_s C_s})/Z_B = Q_F(F - \frac{1}{F})$, where ω_s is the switching angular frequency and the full-load quality factor is $Q_F = \frac{\omega_B L_s}{Z_B}$.

In Fig. 3, the steady-state equivalent circuit with only fundamental components is given. The two fundamental voltage phasors are expressed as

$$\overline{\mathbf{V_{p1N}}} = \frac{4}{\pi}\sin^2\frac{\delta_x}{2}e^{-j90^\circ} \tag{2}$$

$$\overline{\mathbf{V_{s1N}}} = \frac{4M}{\pi}\sin^2\frac{\delta_y}{2}e^{j(-90^\circ-\phi)} \tag{3}$$

where the voltage gain M is defined as

$$M = \frac{n_t V_Y}{V_X}. \tag{4}$$

By using the principle of superposition, the normalized resonant tank current i_{tN} in the time domain can be found as

$$i_{tN}(t) = \sqrt{2}I_{p1N}\sin(\omega_s t - 90^\circ) + \sqrt{2}I_{s1N}\cos(\omega_s t - \phi). \tag{5}$$

In the expression of $i_{tN}(t)$, the first and second terms are the results of the excitation of $\overline{\mathbf{V_{p1N}}}$, $\overline{\mathbf{V_{s1N}}}$, respectively. Then, the normalized rms value of the tank current is calculated as

$$I_{tNr} = \frac{\sqrt{8M^2\sin^4\frac{\delta_y}{2} - 16M\cos\phi\sin^2\frac{\delta_x}{2}\sin^2\frac{\delta_y}{2} + 8\sin^4\frac{\delta_x}{2}}}{\pi X_{sN}}. \tag{6}$$

Assuming a lossless power transfer, the average power P_{oN} can be evaluated from either side of the equivalent circuit, which is given as

$$P_{\text{oN}}(\phi,\delta_x,\delta_y) = \frac{8M}{\pi^2 X_{sN}}\sin^2\frac{\delta_x}{2}\sin^2\frac{\delta_y}{2}\sin\phi = P_{\max}\cdot G \tag{7}$$

where the maximum power is defined as $P_{\max} = \frac{8M}{\pi^2 X_{sN}}$, and the load level index G is defined as $G = P_{oN}/P_{\max} = \sin^2\frac{\delta_x}{2}\sin^2\frac{\delta_y}{2}\sin\phi$. Apparently, the polarity of the average power relies on the polarity of angle ϕ only, while its magnitude is decided by G—the combination of all three phase angles.

As the average power is a function of three variables, a specified control route should be developed to select the optimal set of three angles for power manipulation. Since AAPWM has a favorable nature to keep up to seven switches in ZVS at light load, the specified control route should be selected to reduce conduction loss by operating with the minimum tank current. In this work, the rms tank current is selected as the objective to be optimized, since it is the main factor of conduction loss in switches.

The objective function to optimize the rms tank current can be expressed as

$$\begin{aligned}&\underset{\phi,\delta_x,\delta_y}{\text{Minimize}}\ \ I_{tNr}(\phi,\delta_x,\delta_y)\\ &\text{subject to } G(\phi,\delta_x,\delta_y) = G^\star, -\frac{\pi}{2} < \phi < \frac{\pi}{2}\\ &0 < \delta_x < \pi, 0 < \delta_y < \pi\end{aligned}$$

where $G^\star$ is a specified power level. Since the optimization problem has an equality constraint and several inequality constraints, it can be solved with Karush–Kuhn–Tucker (KKT) conditions [5]. The KKT function $\mathbf{L}$ incorporating all constraints can be written as

$$\begin{aligned}&\mathbf{L}(\phi,\delta_x,\delta_y,\lambda,\boldsymbol{\mu})\\ &= I_{tNr}(\phi,\delta) + \lambda\cdot g(\phi,\delta_x,\delta_y) + \sum_{i=1}^{6}\mu_i\cdot h_i(\phi,\delta_x,\delta_y)\end{aligned}$$

where λ is the KKT multiplier for the equality constraint and μ_i is the KKT multiplier for the inequality constraint. The equality constraint g is defined as

$$g(\phi,\delta_x,\delta_y) = G(\phi,\delta_x,\delta_y) - G^\star. \tag{8}$$

The six inequality constraints are defined as

$$\begin{cases} h_1(\phi,\delta_x,\delta_y) = -\delta_x\\ h_2(\phi,\delta_x,\delta_y) = \delta_x - \pi\\ h_3(\phi,\delta_x,\delta_y) = -\delta_y\\ h_4(\phi,\delta_x,\delta_y) = \delta_y - \pi\\ h_5(\phi,\delta_x,\delta_y) = \phi - \pi/2\\ h_6(\phi,\delta_x,\delta_y) = -\phi - \pi/2. \end{cases} \tag{9}$$

Mathematically, the expected local minimum $(\phi^*,\delta_x^*,\delta_y^*)$ should satisfy the KKT conditions as follows:

$$\begin{cases} \frac{\partial L}{\partial\phi}(\phi^*,\delta_x^*,\delta_y^*) = 0\\ \frac{\partial L}{\partial\delta_x}(\phi^*,\delta_x^*,\delta_y^*) = 0\\ \frac{\partial L}{\partial\delta_y}(\phi^*,\delta_x^*,\delta_y^*) = 0\\ g(\phi^*,\delta_x^*,\delta_y^*) = 0\\ \lambda \neq 0;\ \mu_i \geq 0\\ h_i(\phi^*,\delta_x^*,\delta_y^*) \leq 0\\ \mu_i h_i(\phi^*,\delta_x^*,\delta_y^*) = 0. \end{cases} \tag{10}$$

The procedure to solve the above equations can be found in the Appendix. And the obtained closed-form solution is a piecewise function, which has three parts as follows:

Region I: when $\frac{1}{\sqrt{1-G^2}} > M > \sqrt{1-G^2}$, we have

$$\begin{cases} \delta_x = \delta_y = \pi\\ \phi = \arcsin(G). \end{cases} \tag{11}$$

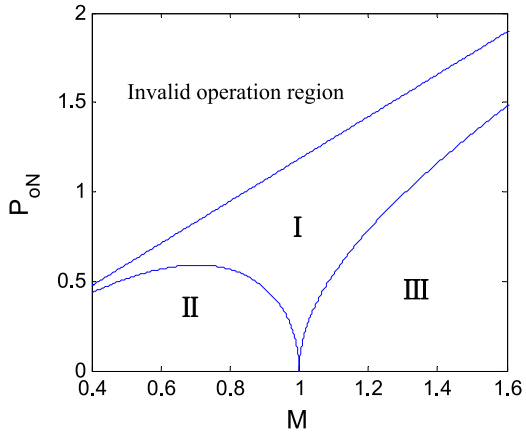

Fig. 4. Three regions for minimum current operation at $F = 1.4$ and $Q_F = 1$.

Region II: when $M < \sqrt{1-G^2}$, or $(G < \sqrt{1-M^2})$, we have

$$\begin{cases} \delta_x = \arccos\left(1 - 2\sqrt{G^2+M^2}\right) \\ \delta_y = \pi \\ \phi = \arctan(\frac{G}{M}). \end{cases} \tag{12}$$

Region III: when $M > \frac{1}{\sqrt{1-G^2}}$, or $(G > \frac{\sqrt{M^2-1}}{M})$, we have

$$\begin{cases} \delta_x = \pi \\ \delta_y = \arccos\left(1 - 2\frac{\sqrt{1+(MG)^2}}{M}\right) \\ \phi = \arctan(MG). \end{cases} \tag{13}$$

Although the PSM plus AAPWM control is adopted at first, it turns out that only the simplified versions in (11)–(13) are needed to achieve minimal rms current operation. In other words, although there are three independent control parameters available, at most two of those three are needed to achieve minimal rms tank current. The solution in (11) for Region I is actually PSM control with both δ_x and δ_y fixed at π [6]. The solution in (12) for Region II is a two-dimensional control method with δ_y fixed at π (i.e., AAPWM is applied on the primary bridge only) [28]. On the other side, (13) for Region III has a fixed δ_x of π and variable δ_y, ϕ. It should be noted that the piecewise solution is applicable to bidirectional power control. Therefore, in both Regions II and III, AAPWM will not be shifted to another bridge when the power direction is reversed. According to the solutions above, the whole P_{oN}–M plane should be divided into three regions in order to apply the minimum rms tank current control, as indicated in Fig. 4. In the case of $M = 1$ (Region I only), PSM control will be the best choice for minimized current operation in the whole load range. In the case of $M \neq 1$, PSM is still the best solution for minimum current operation under the high-power condition. When the average power is reduced to a certain power level, AAPWM should be applied to the bridge on the higher voltage side (Region II or III). To differentiate with the MCT using PSM plus conventional PWM control in [14], the solution given in the current work is referred as the modified minimum current trajectory (M-MCT).

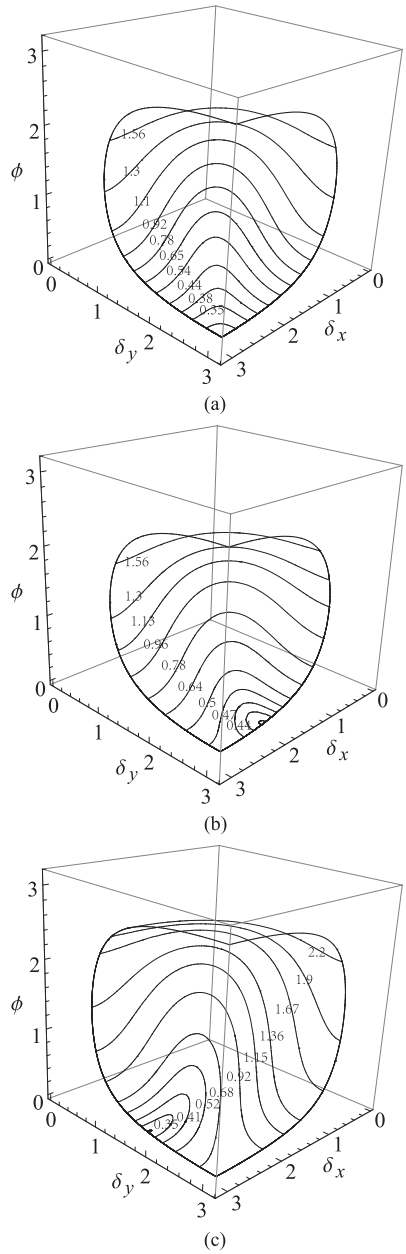

Fig. 5. Tank current contours at a fixed power level in the 3-D space for positive power transfer with $F = 1.4$ and $Q_F = 1$. (a) $M = 1$. (b) $M = 0.8$. (c) $M = 1.5$.

In another angle of view, the searching for M-MCT can be illustrated graphically. In Fig. 5, the variations of the rms tank current with regard to the three phase angles are presented for three regions, respectively. In each subfigure, an equal-power surface ($P_{oN} = 0.3$) is shown for a particular converter gain M. The points of each contour on the power surface have a same normalized rms tank current value, which decreases gradually from top to bottom. It can be seen that those rms current contours tend to shrink to the intersection of two surfaces ($\delta_x = \pi$ and $\delta_y = \pi$) with $M = 1$ [see Fig. 5(a)], which indicates that using PSM control in Region I is able to achieve minimum tank current

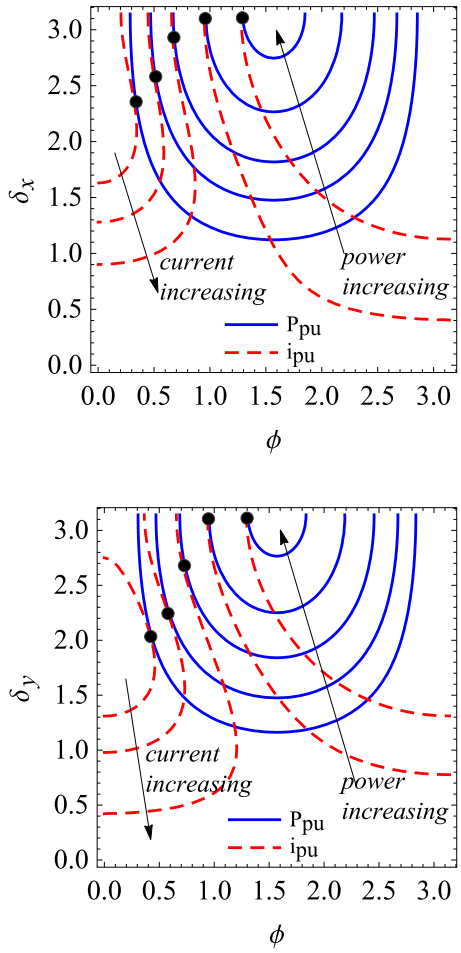

Fig. 6. Searching for the minimum tank current in Region II (left for $M = 0.8$) and Region III (right for $M = 1.5$) for positive power transfer with $Q_F = 1$ and $F = 1.4$.

operation. The same pattern can be viewed too if M is close to 1 and the power level is high enough. In Region II [see Fig. 5(b)] for $M = 0.8$, the minimum current is found to be on the surface of $\delta_y = \pi$, which means that a square wave v_s is necessary to obtain the minimum rms tank current. The similar situation happens for $M = 1.5$ in Region III [see Fig. 5(c)], where $\delta_x = \pi$ or a square-wave voltage v_p is required to achieve the minimum rms tank current. Based on the observations, there is only one control route in Region I due to the single control variable ϕ. However, the minimum current trajectories in other two regions has to be identified since that those have two control variables. Fig. 6 illustrates the principle to find the MCT in the two regions with AAPWM involved. In each region, both the equal-power contours and equal-current contours are drawn together. For each equal-power contour, it has many points of intersection with several different equal-current contours. Only the one which is the tangent point between the two types of contours is the point with the minimum current under a particular power level. Those black dots in the figures form the MCT. It can be seen that the minimum current point is moving toward the boundary of the plane with the increasing of the power level, where the boundary represents PSM control.

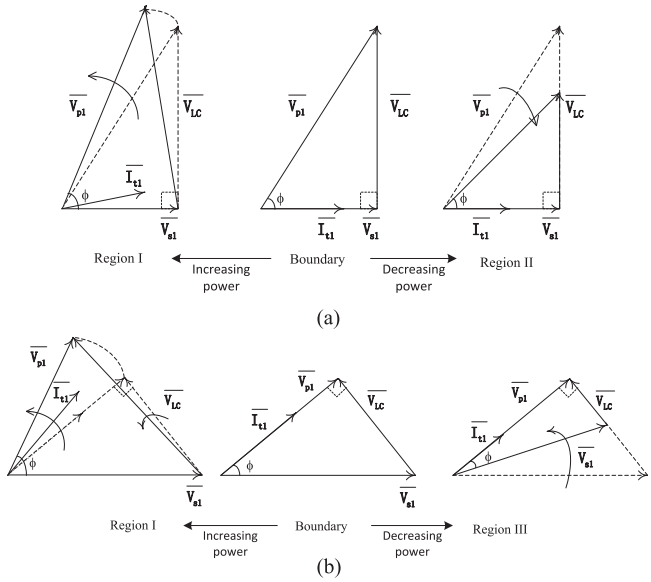

Fig. 7. Phasor diagrams of the M-MCT control strategy for positive power transfer. (a) $M < 1$. (b) $M > 1$.

The boundary conditions in the M-MCT can be found from (11)–(13) as

$$M = \cos\phi, \qquad P_{oN} = \frac{8M\sqrt{1-M^2}}{\pi^2 X_{sN}} \quad \text{Regions I and II} \tag{14}$$

$$M = 1/\cos\phi, \qquad P_{oN} = \frac{8\sqrt{M^2-1}}{\pi^2 X_{sN}} \quad \text{Regions I–III.} \tag{15}$$

(1) At the boundary conditions, the three voltage phasors ($\overline{\mathbf{V_{p1}}}$, $\overline{\mathbf{V_{s1}}}$, and $\overline{\mathbf{V_{LC}}}$) form a right-angled triangle, as shown in Fig. 7. The tank current phasor is in phase with either $\overline{\mathbf{V_{p1}}}$ for $M > 1$ or $\overline{\mathbf{V_{s1}}}$ for $M < 1$.

(2) If the power level is increased from the boundary condition, the steady state moves into Region I and the voltage phasor triangle becomes an acute-angled triangle for both $M < 1$ and $M > 1$. The power is manipulated by increasing the phase-shift angle ϕ between $\overline{\mathbf{V_{p1}}}$ and $\overline{\mathbf{V_{s1}}}$ only.

(3) If the power level is less than the boundary condition, the voltage phasor triangle is kept as a right-angled triangle by manipulating the length of the longer voltage phasor (i.e., reducing the pulsewidth of either v_p for $M < 1$ or v_s for $M > 1$) and the phase-shift angle ϕ at the same time.

With the analytic results obtained above, a series of comparisons between MCT and M-MCT are performed. With the FHA approach, they share the same phasor diagram in Fig. 3 and the same minimum current route in the phasor domain shown in Fig. 7. Both of them have three control variables available to operate the DBSRC along the minimum current route. At a heavy load, there is no need to adjust the pulsewidths of two HF ac voltages, and the effective control scheme only has one dimension. When the load level decreases to a certain values

TABLE I
SOFT SWITCHING IN MCT FOR $M < 1$

Switches	Necessary ZVS conditions
S_1, S_2	$M \sin\left(\phi + \frac{\delta_x}{2}\right) - \sin^2\left(\frac{\delta_x}{2}\right) < 0$
S_3, S_4	$M \sin\left(\phi - \frac{\delta_x}{2}\right) + \sin^2\left(\frac{\delta_x}{2}\right) > 0$
Q_1–Q_4	$M - \sin\frac{\delta_x}{2}\cos\phi > 0$

TABLE II
SOFT SWITCHING IN M-MCT FOR $M < 1$

Switches	Necessary ZVS conditions
S_1	$(1-\cos\delta_x)\cos\delta_x - 2M\cos(\delta_x - \phi) < 0$
S_2, S_3	$(1-\cos\delta_x) - 2M\cos\phi > 0$
S_4	$(1-\cos\delta_x)\cos\delta_x - 2M\cos(\phi + \delta_x) < 0$
Q_1–Q_4	$(1-\cos\delta_x)\cos\phi - 2M < 0$

given in (14) and (15), maximally two out of three control variables are needed for power manipulation. In addition to the interbridge phase shift ϕ, the converter gain that solely decides the pulsewidth of either v_{AB} or v_{CD} should be modulated at a light load. The difference in implementation lies in how to adjust the lengths of the two voltage phasors, either by PWM in MCT or by AAPWM in M-MCT. As a result, they will have different soft-switching performance along the minimum current route. For each switch, the necessary condition of ZVS operation is that the switch current is negative when it is turned ON. Strictly, the actual ZVS range would be smaller than the predicted one because there is a minimum value requirement of turn-ON current to charge/discharge the parasitic/snubber capacitors of the switches. The comparison made here is based on the necessary conditions, with the case of $M < 1(\delta_y = \pi)$ as an example shown in Tables I and II. Unlike the situation in the MCT, the ZVS conditions for the primary bridge in M-MCT do not fall into two groups due to unequal duty cycles. According to those inequalities, the ZVS ranges of all switches under MCT and M-MCT control are illustrated in Fig. 8(a) and (b), respectively, which are plotted with $M < 1$ as an example. The soft-switching boundary of switches is marked with solid blue lines, and the minimum current control route is indicated by the dotted red line. It can be seen that the minimum current routes of both strategies coincide with the ZVS boundary of the secondary-side switches. ZVS operation of all primary switches can be maintained for high-load operation. For the MCT strategy, it is possible to lose ZVS operation of either S_1, S_2 for positive power or S_3, S_4 for negative power at light load. For the M-MCT strategy, S_4 will lose ZVS operation at light load for positive power flow, while S_1 will lose ZVS operation at light load for negative power flow. It can also be found that the load level at which M-MCT loses ZVS operation of one switch is larger than the value at which MCT loses ZVS operation of two switches. The load levels for each strategy losing ZVS can be predicted with the help of Tables I and II. The boundary power of losing ZVS for the MCT is

$$P_{\text{MCT}} = \frac{8M\sqrt{M - M^2}}{\pi^2 Q_F (F - 1/F)}. \tag{16}$$

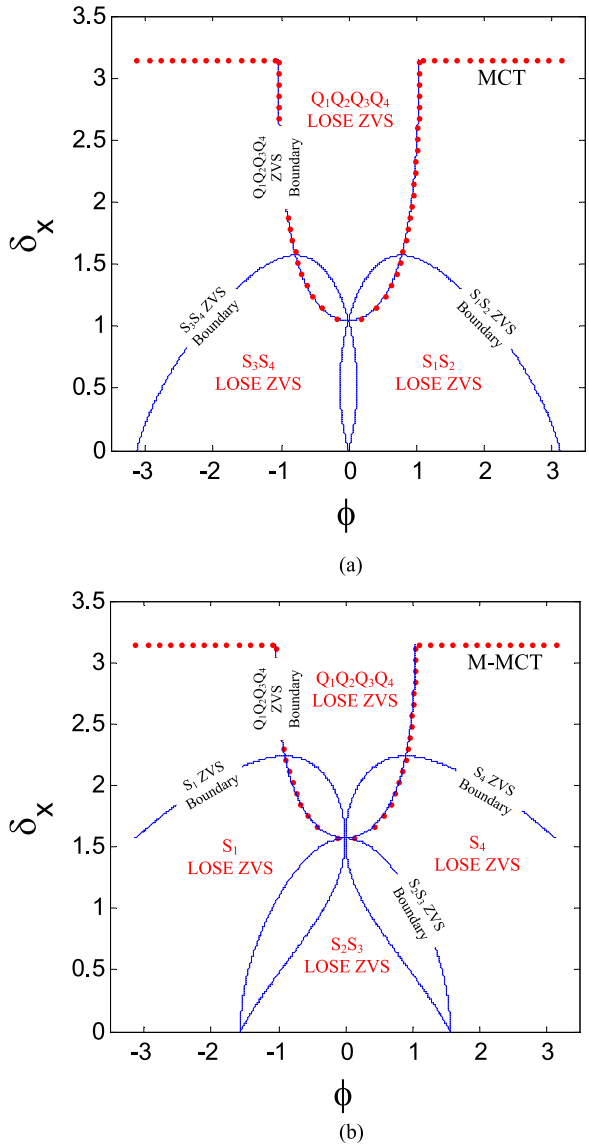

Fig. 8. ZVS range for all switches when $M = 0.8, Q_F = 1$, and $F = 1.4$ under (a) MCT control and (b) M-MCT control.

The boundary power of losing ZVS for the M-MCT is

$$P_{\text{M-MCT}} = \frac{4M\sqrt{V_r^2 - 4M^2}}{\pi^2 Q_F (F - 1/F)} \tag{17}$$

where $V_r = \frac{1+\sqrt{1+8M}}{2}$. The soft-switching situations for $M > 1$ are similar and would not repeated here.

III. VERIFICATION BY EXPERIMENTAL TESTS

To validate the above calculations, a DBSRC is built in the laboratory, and a series of tests have been carried out. The specifications of the prototype converter are as follows: $V_X = 64$–96 V, $V_Y = 88$–104 V, the switching frequency $f_s = 100$ kHz, and the rated power $P_{\text{rate}} = 200$ W.

In this work, the design point is selected at rated power with the maximum converter gain, i.e., the maximum output voltage ($V_{Y\max} = 104$ V) and the minimum input

TABLE III
COMPARISONS OF STEADY-STATE OPERATION AT $M = 0.95$ UNDER M-MCT CONTROL FOR POSITIVE POWER TRANSFER

Power		$\phi(^\circ)$	$\delta_x(^\circ)$	$\delta_y(^\circ)$	$I_{tr}(A)$	$\eta(\%)$
200 W	theory	53.48	180	180	3.99	–
	simulation	53.4	175	175	4.05	–
	experiment	52.8	173	173	4.21	93.99
150 W	theory	37.07	180	180	2.83	–
	simulation	35.4	175	175	2.79	–
	experiment	31.7	173	173	2.87	95.54
100 W	theory	23.69	180	180	1.83	–
	simulation	21.3	175	175	2.06	–
	experiment	17.5	173	173	1.84	96.15
50 W	theory	11.94	160.40	180	0.91	–
	simulation	10.6	160.0	175	0.90	–
	experiment	8.5	160.1	173	0.98	89.29

TABLE IV
COMPARISONS OF STEADY-STATE OPERATION AT $M = 0.54$ UNDER M-MCT CONTROL FOR POSITIVE POWER TRANSFER

Power		$\phi(^\circ)$	$\delta_x(^\circ)$	$\delta_y(^\circ)$	I_{tr}(A)	$\eta(\%)$
200 W	theory	49.33	131.08	180	4.29	–
	simulation	48.1	131.0	175	4.37	–
	experiment	54.6	131.0	173	4.42	92.20
150 W	theory	41.11	115.69	180	3.21	–
	simulation	40.5	115.6	175	3.36	–
	experiment	41.9	115.7	173	3.42	92.00
100 W	theory	30.19	104.45	180	2.14	–
	simulation	28.4	104.4	175	2.34	–
	experiment	27.1	104.4	173	2.45	90.90
50 W	theory	16.22	97.17	180	1.07	–
	simulation	14.0	97.2	175	1.41	–
	experiment	11.2	97.2	173	1.52	89.29

voltage ($V_B = V_{X\min} = 64$ V). The normalized frequency F is selected at 1.4 for above resonance operation with some soft-switching margin. The maximum converter gain is selected at $M_{\max} = 0.95$. Therefore, the transformer turn ratio is

$$n_t : 1 = M_{\max} \cdot V_{X\min} : V_{Y\max} = 0.585{:}1. \tag{18}$$

The base impedance Z_B is

$$Z_B = \frac{n_t^2 V_{Y\max}^2}{P_{\text{rate}}} = 18.48\ \Omega. \tag{19}$$

The full-load quality factor Q_F is chosen to be 1. Then, the parameters of the resonant tank can be calculated as

$$L_s = \frac{Q_F F Z_B}{\omega_s} = 41.18\,\mu\text{H}, \quad C_s = \frac{F}{Q_F Z_B \omega_s} = 120.57\,\text{nF}.$$

The model of the four primary switches is IRFB4620 (200 V, 25 A, and 60 mΩ) and that of the secondary four switches is STP40NF20 (200 V, 40 A, and 45 mΩ). The transformer is built with a ETD-34 Ferrite core whose material is N97. The actual turn ratio is 10:17. The total measured leakage inductance reflected to the primary side is around 5 μH, which can be counted as part of L_s. The magnetizing inductance is found to be around 1.18 mH, which is large enough to be neglected. With M-MCT control, the prototype converter is tested with two

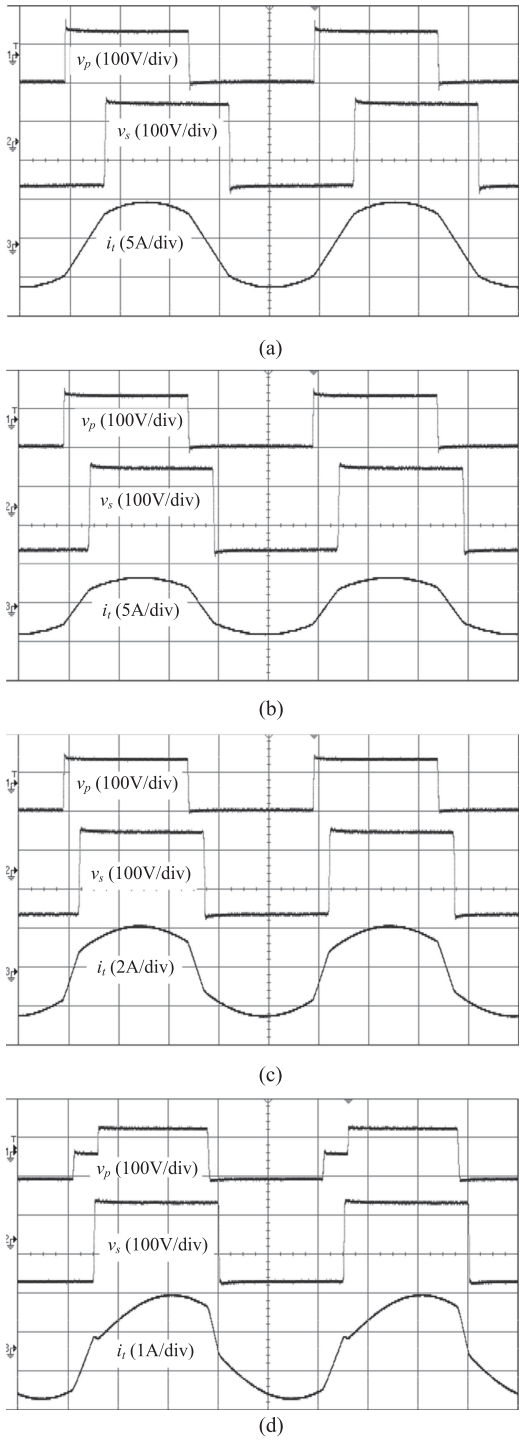

Fig. 9. Measured waveforms of the M-MCT at different load levels when $M = 0.95$ for positive power transfer. (a) 100% load. (b) 75% load. (c) 50% load. (d) 25% load.

different values of the converter gain: the maximum gain at 0.95 ($V_X = 64$ V and $V_Y = 104$ V) and the minimum gain at 0.54 ($V_X = 96$ V and $V_Y = 88$ V). The measured data are collected in Tables III and IV, respectively, to be compared with values obtained from theoretical calculation and simulation to validate the FHA-based analysis. The simulation results are obtained from PSIM software, in which the deadband between the gating

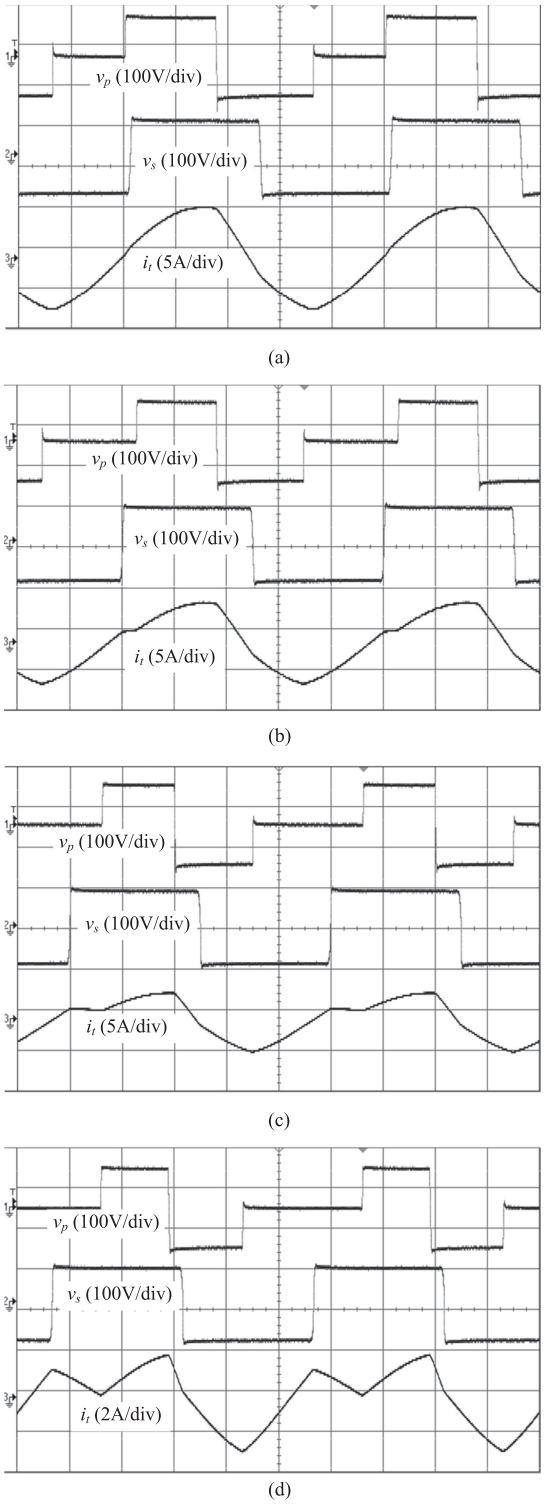

Fig. 10. Measured waveforms of the M-MCT at different load levels when $M = 0.54$ for positive power transfer. (a) 100% load. (b) 75% load. (c) 50% load. (d) 25% load.

signals of two switches in same bridge arm is set at 5°. It can be seen that the values of important control variables and rms current from calculation, simulation, and experiment show good consistency. The highest efficiency 96.15% is obtained at 100 W

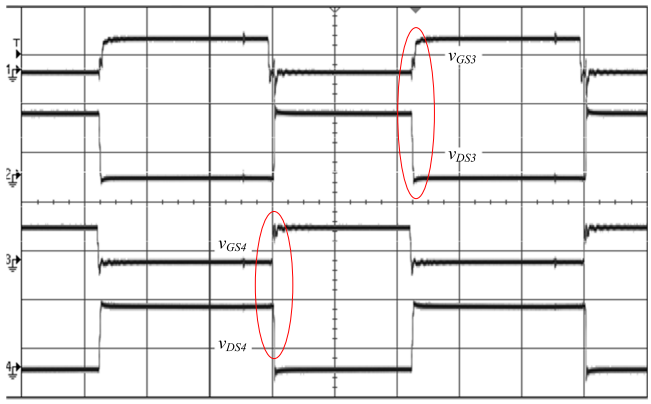

Fig. 11. Switching behavior of S_3 and S_4 at light load.

for $M = 0.95$, which is measured by using a Yokogawa WT500 power analyzer.

The recorded waveforms of different power levels are presented in Figs. 9 and 10 for different gains. In each case, the three waveforms recorded from top to bottom are v_p, v_s, and i_t, respectively. The boundary power for $M = 0.95$ is found to be 77.7 W according to (14). Therefore, when $M = 0.95$, the effect of AAPWM is only visible from the waveform of v_p under 25% load (50 W) in Region II [see Fig. 9(d)], while all higher load cases are operating in Region I with the conventional PSM [see Fig. 9(a) and (c)]. When $M = 0.54$, The boundary power is found as 267.9 W. Thus, the converter works in Region II for all test conditions, as shown in Fig. 10, which can be identified from the waveforms of v_p.

With the application of AAPWM, ZVS operation of switch S_4 can be lost at light load as predicted. Fig. 11 presents the gating signals and switch voltages of S_3 and S_4 together. It is clearly seen that the duty cycle of S_3 is larger than that of S_4. And S_3 can be turned ON with zero voltage, while S_4 cannot.

To demonstrate the feature of bidirectional power flow, the negative power operation with $M = 0.95$ under M-MCT control is also tested, and the waveforms are given in Fig. 12. Based on the principle of M-MCT control in (11)–(13), the AAPWM is still applied on the primary side, though the primary side is consuming power now. The operation waveforms look almost symmetric to those of positive power operation. The experimental tests are all performed in an open-loop manner. To implement the strategy in the closed loop, the dc voltages on both sides are needed to be monitored, which will be used to calculate the actual converter gain. Once a new power command is received, it should be compared with the current power level. If the power difference is larger than a preset threshold value, new control angles should be calculated based on (11)–(13). The calculation may be performed in real time or by referring to a stored lookup table. The execution of the adjustment of control angles should be integrated with some voltage/current stabilization controllers for better transient performance, which are to be addressed in separated works.

Some comparisons are also performed among the conventional PSM, the MCT control, and the proposed M-MCT control strategy through a series of experimental tests on the same

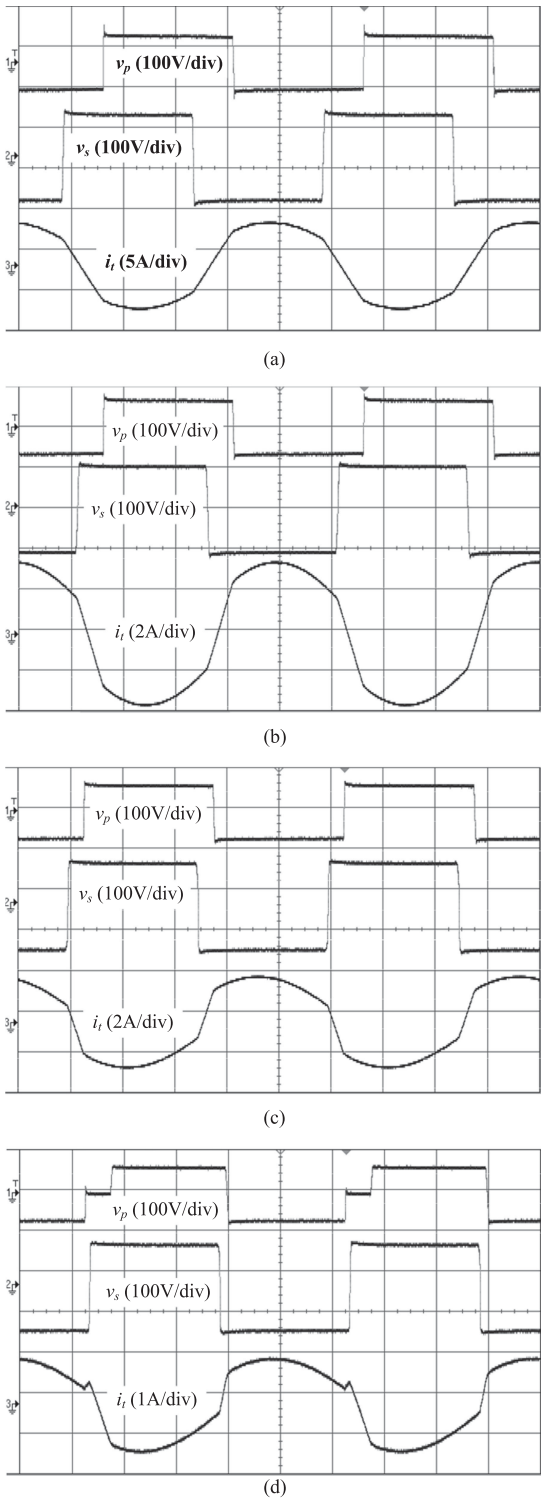

Fig. 12. Measured waveforms of the M-MCT at different load levels when $M = 0.95$ for negative power transfer. (a) 100% load. (b) 75% load. (c) 50% load. (d) 25% load.

converter prototype. With $M = 0.95$, the measured rms tank currents at different load levels are compared in Fig. 13(a). For 100%, 75%, and 50% load operation, the rms currents are same because the used control parameters are exactly the same under PSM, MCT, and M-MCT. For 25% load operation, the measured

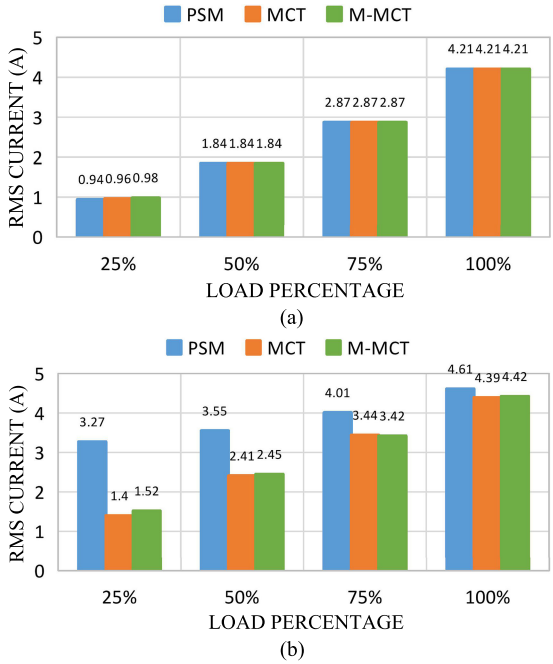

Fig. 13. Measured rms tank currents at different load levels with PSM, MCT, and M-MCT control for positive power transfer. (a) $M = 0.95$. (b) $M = 0.54$.

rms currents are almost same too even though the pulsewidth of v_p is modulated by PWM under MCT or AAPWM under the M-MCT. Therefore, there is no apparent difference in conduction loss among the three control methods. At 25% load, ZVS is still maintained for all switches under PSM, since the converter gain is quite close to 1. Under the MCT strategy, both S_3 and S_4 lost ZVS operation, and only S_4 lost ZVS operation under the M-MCT strategy. As the switching loss is proportional to the square of the switch voltage, the total switching losses under three strategies in a decreasing order are MCT, M-MCT, and PSM. The efficiency of PSM at 25% load is found to be higher than that of the other two cases, as shown in Fig. 14(a).

With $M = 0.54$, both MCT and M-MCT show apparent advantages over PSM in terms of the rms tank current and the overall efficiency. Even though the existence of high-order current harmonics makes the actual rms tank current higher than the calculated values for both MCT and M-MCT strategies, those are still lower than that of the PSM strategy [see Fig. 13(b)]. Consequently, the conduction loss becomes the dominant portion of the total loss in PSM control. The theoretical rms current is exactly the same for the MCT and the M-MCT, since the FHA approach is used for the same phasor circuit in Fig. 3. In actual practice, the high-order harmonics will contribute to some deviation between them. PWM will induce odd-order harmonics and AAPWM will induce both odd- and even-order harmonics. The weight of high-order harmonics rises with the decrease in the pulsewidth. On one side, if the pulsewidth of the modulated HF ac voltage is same, the M-MCT would have higher rms current than the MCT. On the other side, the M-MCT requires a wider pulsewidth than the MCT at the same power level, which tends to compensate for the deviation in the rms current. The result of such a tradeoff can be found from Fig. 15, showing the

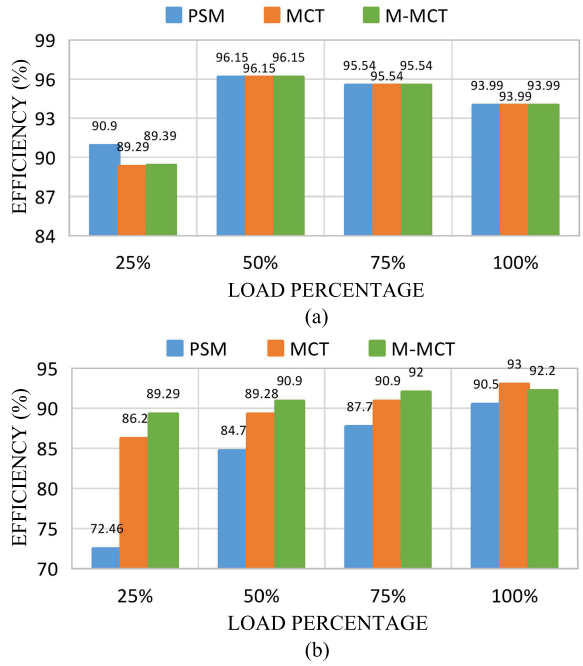

Fig. 14. Measured efficiency at different load levels with PSM, MCT, and M-MCT control for positive power transfer. (a) $M = 0.95$. (b) $M = 0.54$.

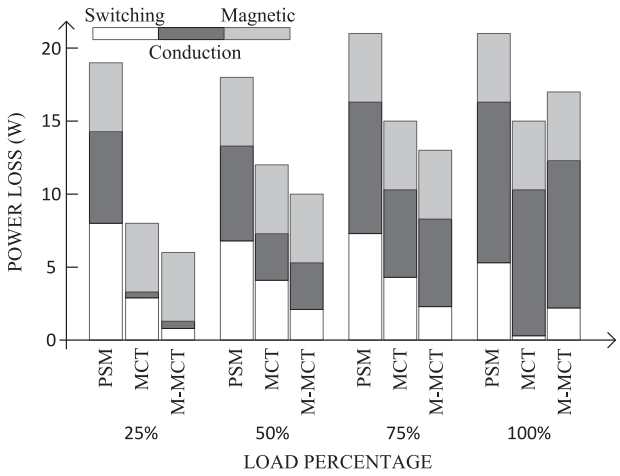

Fig. 15. Breakdown of power loss at $M = 0.54$ for three different control strategies.

breakdown of power loss for three strategies at different load levels under $M = 0.54$. There is no big difference in the rms current between the two MCT strategies, which indicates that they have almost equal conduction loss. Thus, switching loss becomes the key factor affecting the efficiency. At full load, the M-MCT loses ZVS operation of one switch, while the MCT can still maintain full ZVS operation with higher efficiency. At light load, both the MCT and the M-MCT lose full ZVS operation. Then, the efficiency of the M-MCT is better than that of the MCT due to one more switch operating in ZVS.

IV. Conclusion

In this paper, a control strategy, named M-MCT, combining PSM and AAPWM scheme, is applied on a dual-bridge resonant converter. An optimized control route with piecewise closed-form solutions is found by minimizing the rms tank current. It is found that the AAPWM scheme is only needed in one of the two bridges depending on the converter gain to achieve the minimum tank current. Performance comparisons with PSM and the PWM-based MCT strategy were carried out. It can be concluded that the introduction of PWM and AAPWM is helpful to reduce switching loss by maintaining more switches with a wider ZVS operation range at light load as well. Although more high-order harmonics will be resulted from the AAPWM-based M-MCT, the measured conduction loss does not increase significantly compared with the PWM-based MCT at the same power level. This is due to the fact that AAPWM-generated HF voltages have wider pulsewidth than that of PWM-generated voltages at the same power level, and the weight of high-order harmonics decreases with the increase of the pulsewidth. To make use of the favorable nature of wide ZVS range and achieve better performance, the M-MCT strategy is recommended to high-voltage low-current applications, in which the weight of switching loss in the total loss is more than that of conduction loss. In future work, more efforts will be put on the influences of high-order harmonics on the ZVS operation range, by which the converter design could be optimized to further improve the converter efficiency.

Appendix

By solving (10), the following equations are obtained:

$$\begin{cases} \frac{2M}{\sin\phi\cos\phi} + \lambda G = 0 \\ (2\sin^4\frac{\delta_x}{2} + \lambda G)\sin\delta_x = 0 \\ (2M^2\sin^4\frac{\delta_y}{2} + \lambda G)\sin\delta_y = 0. \end{cases} \tag{20}$$

Through careful analysis, there are two groups of possible solutions available. The first group is

$$\begin{cases} \frac{2M}{\sin\phi\cos\phi} + \lambda G = 0 \\ 2\sin^4\frac{\delta_x}{2} + \lambda G = 0 \\ \sin\delta_y = 0. \end{cases} \tag{21}$$

With the help of (7), the following two equations can be found:

$$M = \cos\phi\sin^2\frac{\delta_x}{2} \tag{22}$$

$$G = \tan\phi \cdot M. \tag{23}$$

Simplifying the above two equations yields the solution of Region II shown in (12). Additionally, (22) reveals that the solution is only valid for $M < 1$. According to (23), ϕ has to be raised to increase the power level G when M is fixed. Then, $\sin^2\frac{\delta_x}{2}$ has to be raised too according to (22). However, the maximum of $\sin^2\frac{\delta_x}{2}$ is 1 at $\delta_x = \pi$, which indicates the boundary of Region II. The boundary can be found as (14) by substituting $\delta_x = \pi$ into (22) and (23).

The second group of solutions is

$$\begin{cases} \frac{2M}{\sin\phi\cos\phi} + \lambda G = 0 \\ \sin\delta_x = 0 \\ 2M^2 \sin^4\frac{\delta_y}{2} + \lambda G = 0. \end{cases} \tag{24}$$

With the help of (7), the following two equations can be found:

$$1/M = \cos\phi \sin^2\frac{\delta_y}{2} \tag{25}$$

$$G = \tan\phi/M. \tag{26}$$

Simplifying the above two equations yields the solution of Region III shown in (13). Additionally, (25) reveals that the solution is only valid for $M > 1$. According to (26), ϕ has to be raised to increase the power level G when M is fixed. Then, $\sin^2\frac{\delta_y}{2}$ has to be raised too according to (25). However, the maximum of $\sin^2\frac{\delta_y}{2}$ is 1 at $\delta_y = \pi$, which indicates the boundary of Region III. The boundary can be found as (15) by substituting $\delta_y = \pi$ into (25) and (26). Finally, it is seen that Region I is formed as the common part of Regions II and III due to the limitation of δ_x and δ_y.

REFERENCES

[1] R. L. Steigerwald, "A comparison of half-bridge resonant converter topologies," *IEEE Trans. Power Electron.*, vol. 3, no. 4, pp. 174–182, Apr. 1988.

[2] B. Yang, F. C. Lee, A. J. Zhang, and G. Huang, "LLC resonant converter for front end DC/DC conversion," in *Proc. IEEE Appl. Power Electron. Conf. Expo*, 2002, pp. 1108–1112.

[3] A. K. S. Bhat, "Analysis and design of LCL-type series resonant converter," *IEEE Trans. Ind. Electron.*, vol. 41, no. 1, pp. 118–124, Feb. 1994.

[4] M. K. Kazimierczuk and D. Czarkowski, *Resonant Power Converters*. New York, NY, USA: Wiley, 2012.

[5] S. J. Wright and J. Nocedal, *Numerical Optimization*, vol. 2. New York, NY, USA: Springer, 1999.

[6] X. Li and A. K. S. Bhat, "Analysis and design of high-frequency isolated dual-bridge series resonant dc/dc converter," *IEEE Trans. Power Electron.*, vol. 21, no. 2, pp. 850–862, Apr. 2010.

[7] X. Li, "A LLC-type dual-bridge resonant converter: Analysis, design, simulation, and experimental results," *IEEE Trans. Power Electron.*, vol. 29, no. 8, pp. 4313–4321, Aug. 2014.

[8] T. Jiang, J. Zhang, X. Wu, K. Sheng, and Y. Wang, "A bidirectional LLC resonant converter with automatic forward and backward mode transition," *IEEE Trans. Power Electron.*, vol. 30, no. 2, pp. 757–770, Nov. 2015.

[9] Y. Du, S. M. Lukic, B. S. Jacobson, and A. Q. Huang, "Modulation technique to reverse power flow for the isolated series resonant DC-DC converter with clamped capacitor voltage," *IEEE Trans. Power Electron.*, vol. 59, no. 12, pp. 4617–4628, Dec. 2012.

[10] F. Ibanez, J. M. Echeverria, and L. Fontan, "Novel technique for bidirectional series-resonant DC/DC converter in discontinuous mode," *IET Power Electron.*, vol. 6, no. 5, pp. 1019–1028, 2013.

[11] H. Wu, K. Sun, Y. Li, and Y. Xing, "Fixed-frequency PWM-controlled bidirectional current-fed soft-switching series-resonant converter for energy storage applications," *IEEE Trans. Ind. Electron.*, vol. 64, no. 8, pp. 6190–6201, Aug. 2017.

[12] W. L. Malan, D. M. Vilathgamuwa, and G. R. Walker, "Modeling and control of a resonant dual active bridge with a tuned CLLC network," *IEEE Trans. Power Electron.*, vol. 31, no. 10, pp. 7297–7310, Oct. 2016.

[13] J. Wu, Y. Li, X. Sun, and F. Liu, "A new dual-bridge series resonant DC-DC converter with dual tank," *IEEE Trans. Power Electron.*, vol. 33, no. 5, pp. 3884–3897, May 2018, doi: 10.1109/TPEL.2017.2723640.

[14] L. Corradini, D. Seltzer, D. Bloomquist, R. Zane, D. Maksimovic, and B. Jacobson, "Minimum current operation of bidirectional dual-bridge series resonant DC/DC converters," *IEEE Trans. Power Electron.*, vol. 27, no. 7, pp. 3266–3276, Jul. 2012.

[15] H. Bai and C. Mi, "Eliminate reactive power and increase system efficiency of isolated bidirectional dual-active-bridge dc-dc converters using novel dual-phase-shift control," *IEEE Trans. Power Electron.*, vol. 23, no. 6, pp. 2905–2914, Nov. 2008.

[16] B. Zhao, Q. Song, and W. Liu, "Efficiency characterization and optimization of isolated bidirectional dc-dc converter based on dual-phase-shift control for dc distribution application," *IEEE Trans. Power Electron.*, vol. 28, no. 4, pp. 1711–1727, Apr. 2013.

[17] F. Krismer and J. W. Kolar, "Efficiency-optimized high-current dual active bridge converter for automotive applications," *IEEE Trans. Ind. Electron.*, vol. 59, no. 7, pp. 2745–2760, Jul. 2012.

[18] F. Krismer and J. W. Kolar, "Closed form solution for minimum conduction loss modulation of DAB converters," *IEEE Trans. Power Electron.*, vol. 27, no. 1, pp. 174–188, Jan. 2012.

[19] A. K. Jain and R. Ayyanar, "PWM control of dual active bridge: Comprehensive analysis and experimental verification," *IEEE Trans. Power Electron.*, vol. 26, no. 4, pp. 1215–1227, Apr. 2011.

[20] B. Zhao, Q. Song, W. Liu, G. Liu, and Y. Zhao, "Universal high-frequency link characterization and practical fundamental-optimal strategy for dual-active-bridge dc-dc converter under PWM plus phase-shift control," *IEEE Trans. Power Electron.*, vol. 30, no. 12, pp. 6488–6494, Dec. 2015.

[21] W. Choi, K. M. Rho, and B. H. Cho, "Fundamental duty modulation of dual-active-bridge converter for wide-range operation," *IEEE Trans. Power Electron.*, vol. 31, no. 6, pp. 4048–4064, Jun. 2016.

[22] F-S. Hamdad and A. K. S. Bhat, "A novel pulsewidth control scheme for fixed-frequency zero-voltage-switching DC-to-DC PWM bridge converter," *IEEE Trans. Ind. Electron.*, vol. 48, no. 1, pp. 101–110, Jan. 2001.

[23] A. K. S. Bhat and F. Luo, "A new gating scheme controlled soft-switching DC-to-DC bridge converter," in *Proc. 5th Int. Conf. Power Electron. Drive Syst.*, 2003, pp. 8–15.

[24] Y. Chen and Y. Kang, "An improved full-bridge dual-output dc-dc converter based on the extended complementary pulsewidth modulation concept," *IEEE Trans. Power Electron.*, vol. 26, no. 11, pp. 3215–3229, Nov. 2011.

[25] S. Bhowmick and A. K. S. Bhat, "A fixed-frequency LCC-type resonant converter with inductive output filter using a modified gating scheme," in *Proc. Int. Conf. Adv. Energy Convers. Technol.*, 2014, pp. 140–145.

[26] C. Yu and K. Yong, "An improved full-bridge dual-output DC-DC converter based on the extended complementary pulse width modulation concept," *IEEE Trans. Power Electron.*, vol. 26, no. 11, pp. 3215–3229, Nov. 2011.

[27] N. Harischandrappa and A. K. S. Bhat, "A fixed-frequency LCL-type series resonant converter with a capacitive output filter using a modified gating scheme," *IEEE Trans. Ind. Appl.*, vol. 50, no. 6, pp. 4056–4064, Nov./Dec. 2014.

[28] H. Chen and A. K. S. Bhat, "Analysis and design of a dual-bridge series resonant DC-to-DC converter for capacitor semi-active battery-ultracapacitor hybrid storage system," in *Proc. IEEE 23rd Int. Symp. Ind. Electron.*, 2014, pp. 1788–1793.

Song Hu (S'17) received the B.Eng. degree in electrical engineering from Soochow University, Suzhou, China, in 2013, and the M.S. degree from the Macau University of Science and Technology, Macau, China, in 2015, where he is currently working toward the Ph.D. degree.

His current research interests include high-frequency power converters and its applications.

Xiaodong Li (S'02–M'09–SM'12) received the B.Eng. degree in electrical engineering from Shanghai Jiao Tong University, Shanghai, China, in 1994, and the M.A.Sc. and Ph.D. degrees in electrical engineering from the University of Victoria, Victoria, BC, Canada, in 2004 and 2009, respectively.

From 1994 to 2002, he was an Electrical Engineer with Hongwan Diesel Power Corporation, Zhuhai, China, where he conducted maintenance of the diesel power generation system. He joined the Faculty of Information Technology, Macau University of Science and Technology, Macau, China, in 2009, where he is currently an Associate Professor. His research interests include high-frequency power converters and its applications.

Dr. Li was a recipient of the IEEE Power and Energy Society Best Paper Prize in 2007 and the BOC Excellent Research Award from the Macau University of Science and Technology in 2013.

Ashoka K. S. Bhat (S'82–M'85–SM'87–F'98) received the B.Sc. degree in physics and mathematics from the University of Mysore, Mysore, India, in 1972, the B.E. degree in electrical technology and electronics and the M.E. degree in electrical engineering (both with distinction) from the Indian Institute of Science, Bangalore, India, in 1975 and 1977, respectively, and the M.A.Sc. and Ph.D. degrees in electrical engineering from the University of Toronto, Toronto, ON, Canada, in 1982 and 1985, respectively.

From 1977 to 1981, he was a Scientist in the Power Electronics Group, National Aeronautical Laboratory, Bangalore, and was responsible for the completion of a number of research and development projects. After working as a Postdoctoral Fellow for a short time, he joined the Department of Electrical Engineering, University of Victoria, Victoria, BC, Canada, in 1985, where he is currently a Professor of electrical engineering and is involved in teaching and conducting research in the area of power electronics. He was responsible for the development of the electromechanical energy conversion and power electronics courses and laboratories with the Department of Electrical Engineering, University of Victoria.

Dr. Bhat was a recipient of the Excellence in Teaching Award from the Faculty of Engineering during the year 2008 and the Wighton Fellowship for the year 2010. He is a Fellow of the Institution of Electronics and Telecommunication Engineers (India) and a registered Professional Engineer in the province of British Columbia, Canada.